01 Aug 2023

# Outgassing Behavior and Heat Treatment Optimization of JSC-1A Lunar Regolith Simulant

Ryan P. Wilkerson

Mihail P. Petkov

Gerald E. Voecks

Catherine S. Lynch

*et. al. For a complete list of authors, see https://scholarsmine.mst.edu/chem_facwork/3375*



## Recommended Citation

R. P. Wilkerson et al., "Outgassing Behavior and Heat Treatment Optimization of JSC-1A Lunar Regolith Simulant," *Icarus*, vol. 400, article no. 115577, Elsevier, Aug 2023.
The definitive version is available at https://doi.org/10.1016/j.icarus.2023.115577

Icarus 400 (2023) 115577

Contents lists available at ScienceDirect

Icarus

journal homepage: www.elsevier.com/locate/icarus

# Outgassing behavior and heat treatment optimization of JSC-1A lunar regolith simulant

Ryan P. Wilkerson [a,b,*], Mihail P. Petkov [g], Gerald E. Voecks [g], Catherine S. Lynch [c], Holly S. Shulman [c,d], Santhoshkumar Sundaramoorthy [e], Amitava Choudhury [e], Douglas L. Rickman [f], Michael R. Effinger [b]

[a] Los Alamos National Laboratory, Los Alamos, NM, 87545, United States of America
[b] NASA Marshall Space Flight Center, Huntsville, AL 35812, United States of America
[c] Alfred University, Alfred, NY 14802, United States of America
[d] DrHollyShulman, LLC, Belmont, NY 14813, United States of America
[e] Department of Chemistry, Missouri University of Science and Technology, Rolla, MO 65409, United States of America
[f] Jacobs Engineering, Inc., Huntsville, AL 35812, United States of America
[g] NASA Jet Propulsion Laboratory, California Institute of Technology, Pasadena, CA 91109, United States of America

ARTICLE INFO

*Keywords:*
Mineralogy
Moon
Moon, surface
Geological processes

ABSTRACT

As NASA strives towards a long duration presence on the Moon, it has become increasingly important to learn how to better utilize resources from the lunar surface for everything from habitats, vehicle infrastructure, and chemical extraction. To that end, a variety of lunar simulants have been sourced from terrestrially available volcanic minerals and glass as Apollo regolith is unavailable for experimentation needing large masses. However, while mineralogy and chemical composition can approach that of lunar material in these simulants, there are still distinct non-lunar phases such as hydrates, carbonates, sulfates, and clays that can cause simulants to behave distinctly non-lunar in a variety of processing conditions that maybe applied in-situ to lunar material. Notably, severe glassy bubbling has been documented in a variety of vacuum sintering experiments on JSC-1A lunar mare simulant heated via microwaves. The origins of this outgassing have not been well understood but are normally attributed to the decomposition of non-lunar contaminates intrinsic to virtually all terrestrially sourced simulants. As such, a series of controlled environmental tests were performed to ascertain the origins of the high temperature outgassing and to develop heat treatments that can drive JSC-1A closer to lunar composition and behavior. It was found that in JSC-1A at elevated temperatures distinct gas evolutions of water, carbon dioxide, and sulfur dioxide occur in both inert gas and vacuum. Additionally, the presence of hydrogen during heat treatments was shown to dramatically change gas evolutions, leading to distinctly more lunar-like composition and behavior from JSC-1A simulant.

## 1. Introduction

Compared to the Apollo missions in the 1960s and 1970s, NASA's planned return to the Moon will require vastly more mass from Earth and technologies that have never been tested on the Moon (NASA, 2020). Success in the Artemis program will require development and testing of a complex range of equipment on Earth using conditions that adequately replicate the lunar environment, i.e. vacuum ($\sim 10^{-13}$–$10^{-15}$ bar), radiation, and crushed rock (NASA, 2019). That crushed lunar rock, termed "regolith", is derived from the original lithologies of the Moon by hypervelocity impacts over the life of the Moon.

During the Apollo missions, dust from rocket plumes and travel on the Moon was lofted in the landing area. To mitigate the dust lofting and create a sustaining work environment the construction of landing/launch pads, roads, and habitats will be required. This construction will utilize regolith for raw material, dubbed in-situ resource utilization (ISRU). Recently in the theme of ISRU, new technology is being developed to explore the use of lunar regolith for construction projects utilizing sintering (Song et al., 2020; Taylor and Meek, 2005; Whittington

* Corresponding author at: Los Alamos National Laboratory, Los Alamos, NM, 87545, United States of America
*E-mail address:* rwilkerson@lanl.gov (R.P. Wilkerson).

https://doi.org/10.1016/j.icarus.2023.115577
Received 27 February 2023; Received in revised form 29 March 2023; Accepted 4 April 2023
Available online 6 April 2023

and Parsapoor, 2022; Zocca et al., 2020), 3D printing (Goulas and Friel, 2016; Howe et al., 2014; Taylor et al., 2018), and chemical extraction (Allen et al., 1996; Metzger et al., 2020; Schlüter and Cowley, 2020). The Apollo missions returned a total of 382 kg of lunar regolith from six different landing sites (Vaniman et al., 1991). This is at least an order of magnitude less material than Artemis is going to need to perform pre-flight tests of equipment. Hence, testing of equipment that is going to the Moon will have to be done with lunar regolith simulants, further complicating the situation.

The original lunar rock types are similar to certain basaltic igneous rocks found on Earth. However, there are distinct differences between the two. The lunar regolith was created by hypervelocity impacts into an airless body over billions of years. Rocks on Earth are more oxidized than lunar norms and in contrast with lunar rocks, terrestrial rocks have existed in an environment with $H_2O$ present. Finally, the geology of the Earth has evolved substantially over the life of the planet. It is part of the simulant producer's responsibility to maximize the similarity of their products while minimizing their differences with the lunar regolith.

One of the most widely referenced lunar simulant is JSC-1A. 31 tons of this simulant were made in 2006 and widely distributed. It, and other simulants in the JSC series, are made from a basaltic volcanic ash quarried from the Merriam Crater, Flagstaff, Arizona (Allen, 1993; Gustafson, 2009). The mineralogy of the original ash (as erupted), and the simulant, is relatively simple: roughly equal amounts of labradorite-bytownite plagioclase feldspar and glass, lesser clinopyroxene and olivine, with <1% cumulative of high titanium magnetite, chromite, ilmenite, and pyrite (Schrader et al., 2008). All of these are within lunar mare norms, which consists of plagioclase feldspar, clinopyroxene, olivine, and glass with <1% ilmenite, spinels, troilite, and metallic iron. However, underlying composition of these minerals varies from lunar standard. Lunar plagioclases are generally much richer in calcium (anorthite) than is typical terrestrially, while lunar mare olivines and pyroxenes are iron rich in comparison, with more in the $Fe^{2+}$ oxidation state due to the reducing conditions of the lunar environment (Papike et al., 1991). Additionally, the Merriam Crater ash was exposed to Earth's atmospheric processes for approximately 20,000 years (Duffield et al., 2006). The volcanic minerals and glass, stable at the temperatures and pressures inside a volcano, were not stable in the new environment and weathering began.

As explained in introductory geology texts dealing with rock weathering (Bland and Rolls, 1998), some of the original phases in the ash were converted to new phase that are stable in the weathering environment. These new phases, frequently being hydrated, are unlike lunar mineralogy. In the case of Merriam Crater, a soil profile called caliche started forming. This involves the production of such minerals as clays, carbonates, sulfates, and hydrated oxides. These weathering minerals are mechanically softer than the original minerals, and commonly coat the outer surface of the original ash particles. The total mass of these non-lunar minerals is constrained by the measured loss-on-ignition (LOI) of 0.71. LOI is easily volatilized mass on heating into the range 900°C to 1000°C (McKay et al., 1994).

Providing simulants to validate these aforementioned consolidation processes that involve high temperatures and mimic the high vacuum of the moon has revealed certain common problems: bubbling/foaming and expansion observed with a variety of different simulants (Fateri et al., 2019; Lim et al., 2021; Song et al., 2019). While the origin of these problems has not been adequately addressed in the current literature, it is hypothesized that this is potentially due to the nonlunar components that are present in simulants sourced from terrestrial rock. The goal of this study is to perform a detailed analysis of the outgassing products of JSC-1A, and use that to develop a proposed heat treatment procedure to remove nonlunar contaminants common to simulants sourced from the Merriam Crater.

## 2. Materials and methods

To remove the weathering derived minerals, heat treating the simulant was selected as the method of choice for two specific reasons. It is relatively simple to apply; and, it is founded on the recognition that the weathering minerals are stable at Earth surface conditions, not at temperatures at which the volcanic material was formed. In order to establish an effective heat treatment, the simulant had to be characterized before and after heat treating to understand what changed and if it was more lunar like. The following proved particular useful in simulant characterization to establish the heat treatment protocol.

### 2.1. Thermal analysis and mass spectroscopy

Mass loss and speciation of outgassing products of JSC-1A were determined using simultaneous thermogravimetric analysis (TGA) with integrated mass spectroscopy (MS). TGA data were acquired on a SETSYS Evolution (Setaram, Lyon, France) at temperatures ranging from 25 to 1200°C at a constant heating rate of 2.5°C/min under different atmospheric conditions. Inert atmosphere tests were performed under flowing He at 20 ml/min, while reducing atmosphere tests were conducted under flowing a 5%$H_2$/Ar mixture at 20 ml/min. For vacuum runs the TGA was held under a continuous vacuum of $<1 \times 10^{-4}$ mbar using an attached HiCube 80 Eco turbo vacuum (Pfeiffer Vacuum Inc., Nashua NH, USA). Large volume TGA crucibles allowed for specimen sizes of 1500 mg, which was ideal for collecting strong outgassing signals in the simultaneous MS attached to the TGA. This simultaneous mass spectrometry was collected on a quantitative gas analysis (QGA) quadropole mass spectrometer (Hiden Inc., Peterborough NH, USA) for the flowing gas tests.

For vacuum environment MS, JSC-1A was subjected to identical thermal profiles as in the TGA but in a custom furnace assembly. Simulant powder samples weighing ~23 g sealed in quartz tubes were first carefully evacuated through a leak valve to avoid powder bed fluidization. A base vacuum pressure of $\sim 1 \times 10^{-6}$ mbar was attained using a HiCube 80 Eco turbo pump station. The samples were heated with a 2.5°C/min rate up to 1200°C in a vertical tube furnace type F21100 by Barnstead International (Dubuque IA, USA). The furnace was modified with a Watlow (St. Louis MO, USA) EZ-zone PID power control module for enhanced performance. During the experiments, the main pumping line was protected from condensable contamination using an in-line liquid nitrogen ($LN_2$) trap. Mass spectra were acquired in a split-flow scheme between the primary pump ($LN_2$ trap, backed by the turbo pump) and a 130°C-heated gas transfer line to the Pfeiffer OmniStar GSD 320 gas analyzer. The MS was operated in a constant-flow mode in order to minimize conductance imbalance of the split flow due to large pressure variations. To avoid gas consumption (e.g., ion gauge), a MKS Instruments (Andover MA, USA) 901P piezo-transducer / micro-Pirani combination gauge was chosen to monitor the pressure in the MS transfer line. The actual pressure at the sample was related to the micro-Pirani gauge reading by characterizing the split-flow in the relevant gas flow regime using water vapor in lieu of constant gas-load source at the sample location. During experiments, pressure at the sample increased typically from $\sim 1 \times 10^{-6}$ mbar (base pressure) to low-$10^{-4}$ mbar upon closing the MS aperture at the operational value, and peaked in the 0.01–0.1 mbar range during maximum outgassing conditions for raw JSC-1A simulant. The MS constant-flow rate for JSC-1A was set to 100 mbar.l/s for optimizing the MS sensitivity range for the raw simulant without exceeding mid-$10^{-6}$ mbar total pressure. Reported partial pressures values attributed to various constituents do not take into consideration their different ionization efficiencies.

### 2.2. Chemical analysis

While the bulk chemical composition of JSC-1A has been reported elsewhere (Hill et al., 2007), trace chemical analysis was pursued to

analyze loss of carbon and sulfur. This quantification was performed on a CS-800 carbon/sulfur analyzer (Eltra GmbH, Haan, Germany) in triplicate to account for sampling variability. Alloy standards of near equivalent carbon or sulfur content were used to calibrate the system before and after testing.

Additionally, to determine whether there were changes in valency of iron bearing minerals within the bulk of the simulant, Mössbauer spectroscopy was performed. $^{57}$Fe Mössbauer spectra were collected in transmission geometry at room temperature using a conventional constant acceleration spectrometer with a 50 $mC_i$ $^{57}$Co gamma-ray source embedded in a rhodium matrix. The velocity scale of the spectrometer was calibrated using a spectrum from a 27 μm thick α-Fe foil at room temperature (296 K). A functionality in RECOIL (Lagarec and Rancourt, 1997) software was used for taking optimized sample thickness based on the tentative composition. The resulting Mössbauer data were analyzed using Lorentzian profile fitting by RECOIL software. Each spectrum was deconvoluted into several subspectra as judged by the presence of several components of iron species in the sample. The spectral analyses are reported in Table 1 for parameters such as isomer shift (δ), quadrupole splitting ($\Delta E_Q$), hyperfine magnetic field ($H_{eff}$) in case magnetic sextet, relative area of the subspectrum along with the statistical quality of the fittings ($\chi^2$).

### 2.3. Phase analysis (XRD)

Given that elevated temperatures can induce phase transformations, it was important to maintain original volcanic mineral phases in JSC-1A after heat treatment, as these minerals usefully reproduce lunar mineralogy. X-ray diffraction (XRD) was performed on untreated JSC-1A and after the developed heat treatment to validate that no major phase transformations occurred. XRD was performed on an Aeris Research powder diffractometer (Malvern Panalytical, Malvern, UK). The diffractometer used CuKα radiation that was generated at 40 kV and 15 mA. Scans were performed from a 2θ of 10 to 80° over an 8 h period to generate high fidelity patterns. Major XRD peaks were indexed using HighScore (Malvern Panalytical, Malvern, UK) software to powder diffraction files from the PDF-4+ database (International Centre for Diffraction Data: ICDD, Newtown Square PA, USA).

### 2.4. Particle analysis (BET, morphology, PSD, SEM)

One of the major concerns with any elevated temperature treatment of lunar simulant was the potential for significant changes in particle morphology. To study these changes in depth after heat treatment, a robust series of analyses were performed to determine changes in

**Table 1**
Mössbauer fitting parameters and tentative assignment of components in the pristine simulant and simulant treated under different conditions along with their percentage of various components.

| Tentative assignment | Fe sites | Mössbauer parameters | | | | % Area | $\chi^2$ |
|---|---|---|---|---|---|---|---|
| | | CS/δ (mm/s) | Δ or ε (mm/s) | $B_{hf}$ (kOe) | w+ (mm/s) | | |
| | | | Untreated | | | | |
| Olivine M1 Olivine M2 | $Fe^{2+}$ Doublet 1 | 1.15(2) | 3.06(2) | | 0.23(3) | 11.0(5) | |
| | $Fe^{2+}$ Doublet 2 | 1.13(2) | 2.84(2) | | 0.28(2) | 15.4(7) | |
| Diopside M1 Diopside M2 | $Fe^{2+}$ Doublet 3 | 1.16(2) | 2.29(3) | | 0.34(2) | 6.9(8) | 0.59 |
| | $Fe^{2+}$ Doublet 4 | 1.15(3) | 1.91(3) | | 0.42(2) | 11.0(5) | |
| Iron chromite | $Fe^{2+}$ Doublet 5 | 0.89(2) | 1.99(2) | | 0.50(3) | 17.0(9) | |
| $Fe^{3+}$ Glassy | $Fe^{3+}$ Doublet 6 | 0.53(3) | 0.76(2) | | 0.87(3) | 22.1(5) | |
| $Fe^{3+}$ clusters | $Fe^{3+}$ Sextet 1 | 0.50(2) | −0.052(4) | 427.6(9) | 0.33(2) | 16.6(8) | |
| | | | Vacuum heated at 1050°C | | | | |
| Olivine M1 | Doublet 1 | 1.15(3) | 3.04(2) | | 0.24(2) | 13.3(4) | |
| Olivine M2 | Doublet 2 | 1.13(2) | 2.83(3) | | 0.26(3) | 13.3(4) | |
| Diopside M1 | Doublet 3 | 1.21(2) | 2.41(2) | | 0.80(4) | 15.7(5) | 0.83 |
| Diopside M2 | Doublet 4 | 1.15(2) | 1.91(3) | | 0.42(3) | 6.9(3) | |
| Fe3+ Glassy | Doublet 5 | 0.48(3) | 0.85(3) | | 0.66(2) | 5.6(3) | |
| Fe3+ clusters | Sextet 1 | 0.58(4) | −0.084(6) | 363.5(5) | 1.30(9) | 45.3(6) | |
| | | | Heated under He flow at 1050°C | | | | |
| Olivine M1 | Doublet 1 | 1.17(3) | 3.04(2) | | 0.23(4) | 10.1(4) | |
| Olivine M2 | Doublet 2 | 1.14(2) | 2.84(3) | | 0.25(2) | 14.1(6) | |
| Diopside M1 | Doublet 3 | 1.25(2) | 2.55(2) | | 0.71(6) | 18.9(7) | 0.59 |
| Diopside M2 | Doublet 4 | 1.15(3) | 1.91(4) | | 0.44(6) | 9.3(5) | |
| Fe3+ Glassy | Doublet 5 | 0.36(2) | 1.07(3) | | 1.26(9) | 14.6(6) | |
| Fe3+ clusters | Sextet 1 | 0.61(8) | −0.087(8) | 366.3(6) | 0.70(7) | 33.0(8) | |
| | | | Heated under $Ar/H_2$ at 1050°C | | | | |
| Olivine M1 | Doublet 1 | 1.16(2) | 3.01(2) | | 0.24(5) | 24.3(8) | |
| Olivine M2 | Doublet 2 | 1.14(4) | 2.78(3) | | 0.26(3) | 27.4(4) | |
| Diopside M1/M2 | Doublet 3 | 1.20(5) | 1.89(3) | | 0.686(7) | 28.2(4) | |
| Fe2+ species | Doublet 4 | 0.76(3) | 1.34(2) | | 0.29(3) | 5.69(5) | 0.76 |
| Fe3+ species | Doublet 5 | 0.33(3) | 0.83(3) | | 0.20(8) | 2.98(6) | |
| Metallic Fe | Sextet 1 | −0.0035(9) | 0.0020(8) | 329.4(5) | 0.26(2) | 11.34(6) | |
| | | | Heat Treatment (Fig. 4) | | | | |
| Olivine M1 | $Fe^{2+}$ Doublet 1 | 1.16(3) | 3.04(3) | | 0.22(3) | 9.4(3) | |
| Olivine M2 | $Fe^{2+}$ Doublet 2 | 1.14(2) | 2.81(2) | | 0.32(2) | 20.1(2) | |
| Diopside M1 | $Fe^{2+}$ Doublet 3 | 1.12(3) | 2.24(3) | | 0.45(3) | 17(3) | |
| Diopside M2 | $Fe^{2+}$ Doublet 4 | 1.10(2) | 1.77(2) | | 0.52(3) | 20.4(2) | 0.90 |
| Iron chromite | $Fe^{2+}$ Doublet 5 | 0.80(2) | 1.60(3) | | 0.45(2) | 4.1(3) | |
| $Fe^{3+}$ Glassy | $Fe^{3+}$ Doublet 6 | 0.48(3) | 0.70(2) | | 0.91(2) | 16.2(4) | |
| $Fe^{3+}$ clusters | $Fe^{3+}$ Sextet 1 | 0.62(2) | −0.039(4) | 415.3(6) | 0.25(2) | 13.3(3) | |

particle size distribution, surface area, and morphological distribution.

To ascertain the change in particle size distribution (PSD), samples of as received JSC-1A and post-heat treatment JSC-1A were dispersed in deionized water and analyzed via a BLUEWAVE laser diffraction particle size analyzer (Microtrac, Montgomeryville PA, USA). Results were collated as a volumetric distribution.

Given that there is a significant quantity of glass in JSC-1A, it was expected that any heat treatment could lead to softening of said glass, resulting in smoothing of particle surfaces. To ascertain changes in particle surface area BET was performed on JSC-1A before and after heat treatment and the specific surface area (SSA) was calculated using the multipoint Brunauer Emmett Teller (BET) theory. This method observes the change in relative pressure to determine the level of gas adsorbed onto a material to form a monolayer. This creates an isotherm that is used to calculate the specific surface area (Lowell and Shields, 1991).

The SSA of JSC-1A was analyzed using the Gemini VII 2390p analyzer (Micromeritics, GA USA) using the multipoint BET method. The samples were degassed in nitrogen gas at 200°C for 90 min. An 11-point isotherm with partial pressures ranging from 0.05 to 0.3 p/po was generated to determine the SSA for each sample. For surface areas of at or below 1 $m^2$/g, glass filler rods were added to both the balance tube and the sample tube to add compensating volume which allowed for greater precision for nitrogen adsorption. Approximately 3 g of sample was added to the sample tube such that the height of the filler rod was equal to the height of the filler rod in the balance tube.

Particle morphology was expected to change to some degree if differences were seen in the PSD as well as BET, so to better understand how particles were changing on an individual level, dynamic image analysis (DIA) was performed using a Morphologi G3SE (Malvern Panalytical, Malvern, UK). Automated image analysis was performed under 10× optics in triplicate to produce datasets for untreated and treated JSC-1A on the size of ~500,000 individual particles imaged each, providing a variety of shape data. From this shape data for each particle, aspect ratio was determined via Eq. 1:

$$AR = \frac{W}{L} \tag{1}$$

where $AR$ is the aspect ratio, $L$ is the length of the longest axis within the particle and $W$ is the maximum width normal to the $L$ axis. Form factor was also determined via Eq. 2:

$$FF = \frac{4\pi A}{P^2} \tag{2}$$

where $FF$ is the form factor, $A$ is the projected area of the particle, and $P$ is the measured perimeter of the particle (ISO9276-6, 2008). Using these two particle morphology descriptors, contour maps were produced to show the statistical density of particle elongation (aspect ratio) and surface irregularity (form factor), similar to as reported elsewhere (Rickman et al., 2012, 2016; Rickman and Lowers, 2012). However, instead of using a simple bivariant histogram like reported previously, the $AR$ vs. $FF$ space was processed using a Gaussian bivariant kernel density estimate, described in Eq. 3:

$$KDE = \frac{1}{n}\sum_{i=1}^{n} \frac{1}{2\pi w_R w_F} exp\left( -\frac{(R - vR_i)^2}{2w_R^2} - \frac{(F - vF_i)^2}{2w_F^2} \right) \tag{3}$$

where $KDE$ is the kernel density estimate at point ($AR$,$FF$) as they both vary from 0 to 1 in particle morphology space, $vR$ and $vF$ are the $AR$ and $FF$ values of distributed samples used as kernel centers, $w_R$ and $w_F$ are the bandwidth values of the $AR$ and $FF$ scale, and $n$ is the total number of particles. Bandwidth and $KDE$ values were calculated in Matlab (Botev et al., 2010) and contour levels were normalized between both datasets.

For further verification of the differences between particle morphology contours, a difference contour was produced as well using Eq. 4.

$$KDE_d = KDE_{ht} - KDE_{ut} \tag{4}$$

Where $KDE_d$ is the new difference contour, $KDE_{ht}$ is the heat-treated KDE contour (**7B**), and $KDE_{ut}$ is the untreated KDE contour (**7A**). In addition, root mean square error (RMSE) was calculated between all points in the $AR$ vs $FF$ space of the two contours using Eq. 5:

$$RMSE = \sqrt{\frac{1}{n}\sum_{i=1}^{n} (z_{hi} - z_{ui})^2} \tag{5}$$

where $z_{hi}$ is the $i^{th}$ contour value of the heat treated JSC-1A KDE morphology contour, $z_{ui}$ is the corresponding point in the untreated JSC-1A KDE morphology contour, and $n$ is the total number of equivalent points checked between the two contours.

Densities of particles were analyzed using helium pycnometry on a AccuPyc II TEC (Micromeritics, GA USA). Samples were dried in a 110°C drying oven to remove any adsorbed moisture prior to measurement. The pycnometer was calibrated prior to use using a 10 $cm^3$ insert calibration standard, ensuring accuracy in measurement. Measurements were performed using UHP-He as the gas medium, taking 10 measurements total. To determine the density of the sample, the average of the 10 measurements was taken, along with the calculated standard deviation.

Finally, scanning electron microscopy (SEM) with accompanying energy dispersive x-ray spectroscopy (EDS) was performed to validate the particle analysis as well as XRD phase analysis. Powder specimens were mounted in a two-part epoxy in vacuum, and polished to a 1 μm diamond finish. SEM was performed on a 3700 N (Hitachi, Tokyo, Japan) in variable pressure mode to prevent charging effects on the nonconductive epoxy that the powders were mounted in. Images were taken with at a working distance of 10 mm, with the beam at 10 kV voltage and 60 mA probe current, equivalating to an emission current of 83 μA. EDS spectroscopy was collected with a X-Max$^N$ (Oxford Instruments, Abingdon, United Kingdom) silicon drift detector.

## 3. Results

### 3.1. Thermogravimetric analysis

The TGA and accompanying mass spectrometry of JSC-1A up to full vitrification in high vacuum has is shown in Fig. 1. The time derivative thermogravimetric signal (dTG) is particularly informative when correlated with MS signals to identify the origin and composition of different mass loss events. Mass loss below 200°C is attributed to the loss of physisorbed water, exacerbated by the high surface area of as received JSC-1A and the affinity for water to the surfaces of silicate materials. Continued mass loss between 200°C and 500°C looks to consist of predominately $H_2O$, $CO/CO_2$, $SO_2$, and $SO_3$, likely a combination either physisorbed gases or decomposition of low stability carbonates and sulfates. At 500°C and maximizing at around 600°C is a prominent dTG mass loss, aligning with a strong $CO_2$ evolution, which is attributed to the decomposition of a nonlunar trace carbonate such as $CaCO_3$. Mass loss beyond 700°C is comprised almost entirely of sulfur species such as $SO_2$ and $SO_3$, maximizing at 1050–1100°C. This is suspected to be from a sulfate weathering species such as $CaSO_4 \bullet 2H_2O$ (gypsum), the trace presence of which would correlate well with the some of the low temperature $H_2O$ outgassing which can be attributed to dehydration of the $CaSO_4 \bullet 2H_2O$ structure. Soon after this at >1100°C, instability is seen in the dTG signal as well as MS signals which corresponds to vitrification of the mineral phases into a derivative volcanic glass as well as parallels other high temperature vacuum bubbling that has been seen in JSC-1A and other lunar simulants under similar vacuum/temperature conditions.

Knowing that vitrification occurs at >1100°C, three TGA-MS profiles up to 1050°C were performed to determine if gas environment had any impact on evolved gas species and to inform how to build a more ideal

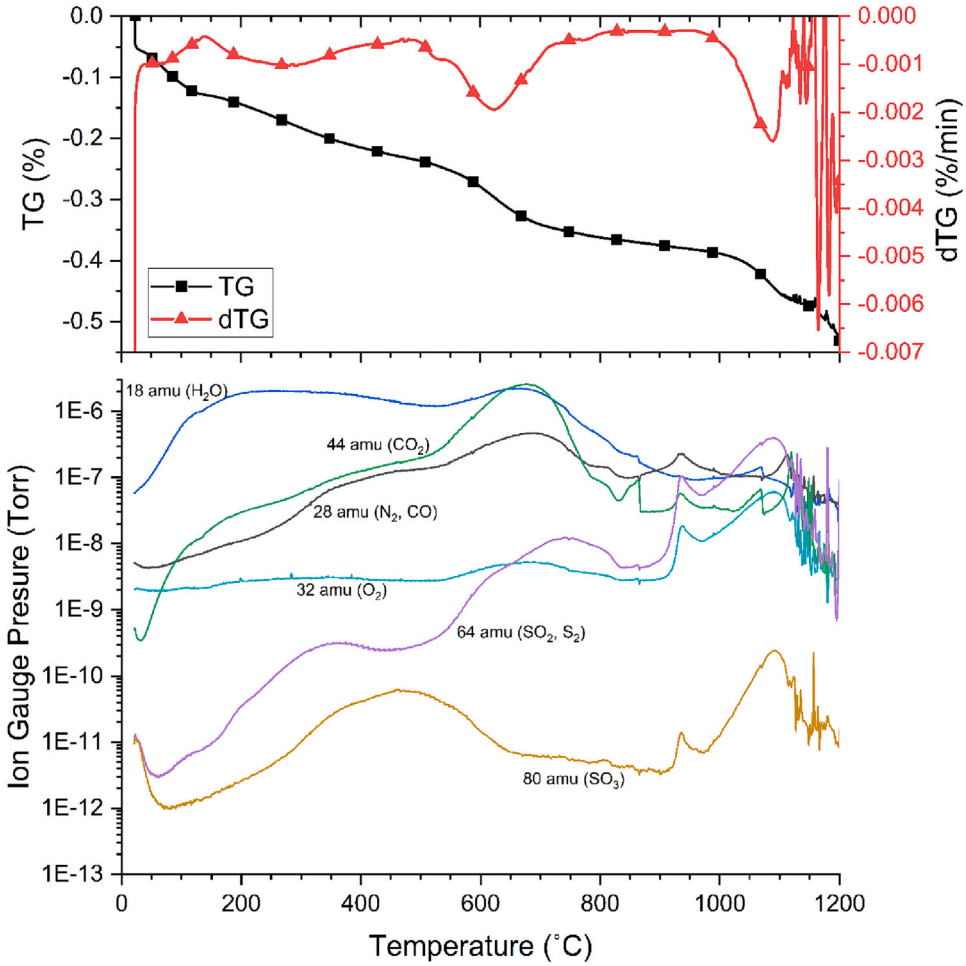


**Fig. 1.** TG-MS of JSC-1A heated beyond vitrification point (~1100°C) in high vacuum of 1E-5 mbar. MS traces are of primary gas evolutions, generally aligning well with peaks in the time derivative (dTG) TG signal. After the vitrification temperature is reached, spiking can be seen in the TG signals as well as the MS signals, which is indicative of unstable bubbling of the glass present within the simulant.

heat treatment profile for JSC-1A. These three profiles can be seen in Fig. 2, with vacuum was kept as a baseline, inert gas (He), and reducing gas (Ar/5$H_2$) to better mimic more commonly accessible gas environments for large scale material treatment. Mass loss events between high vacuum and inert gas are fairly similar, with a much more pronounced loss of water in inert, seen in the dTG signal, which is attributed to some loss of physisorbed water in the vacuum tests prior to test initiation. Total mass loss between inert and vacuum differ by ~0.05 wt%, with the additional loss in vacuum (0.40 wt% vs 0.35 wt% in inert), attributed to more aggressive outgassing of sulfur in the form of $SO_x$ species. The decomposition reaction of sulfate compounds occurs near the highest temperature of the test, and vacuum environments would likely drive reaction favorability towards lower temperatures.

The presence of hydrogen presents a much different decomposition profile, with distinct differences in gas evolution as seen in Fig. 2C. Initial water loss and $CO_2$ evolution occur at identical temperatures to vacuum and inert gas. The first noticeable difference is an overlapping dTG peak at around 750°C which corresponds to a new water evolution as well as a dip in the hydrogen signal which would normally be a "flat" signal as the hydrogen content is constantly refreshing during the test. This is expected to be a sulfate to sulfide reduction event, and the corresponding temperature is around the reported reaction temperature (Kim and Sohn, 2002; Tian et al., 2010) for $CaSO_4$ in $H_2$. This is also supported by the lack of higher temperature $SO_2$ outgassing similar to what is seen in vacuum and inert profiles. The other important feature to note is another water outgassing starting at 750–800°C also mirroring another drop in the hydrogen signal, indicative of another reduction event. This is suspected to be reduction of iron-bearing minerals present in JSC-1A, specifically olivine. Of the constituent oxides that comprise JSC-1A in any major quantity (Hill et al., 2007), iron oxides are the least stable (Siderius et al., 2013) and therefore minerals containing iron oxides would be likely to reduce. This corresponds well with reported observations of $H_2$ reduction of fayalite (Massieon et al., 1993), which is the iron endmember in the olivine group. This is notable, because, if true, it presents a way to produce metallic iron in-situ, potentially enhancing simulant fidelity as a substitution for $nFe^0$ found in lunar regolith (Jolliff et al., 2018).

### 3.2. Chemical analysis

One of the goals of the experimentation is to make meaningful changes to the non-lunar constituents of JSC-1A while maintaining the simulant fidelity. Most of the evolved gas is attributed to carbonate and sulfate weathering species present in the Merriam Crater volcanic source material. Destructive carbon and sulfur analysis of JSC-1A and after the near-vitrification heat treatments can be seen in Table 2. The carbon content of untreated JSC-1A was around 0.025 wt%, with it dropping to between 0.006 and 0.008 wt% after these high temperature treatments. While there was only minor variability of the gas environment on these final carbon content, this loss corresponds to a 67–75% reduction in overall carbon content from the decomposition of carbonate species. Sulfur also saw a reduction from 0.010 wt% to 0.004–0.005 wt%, with

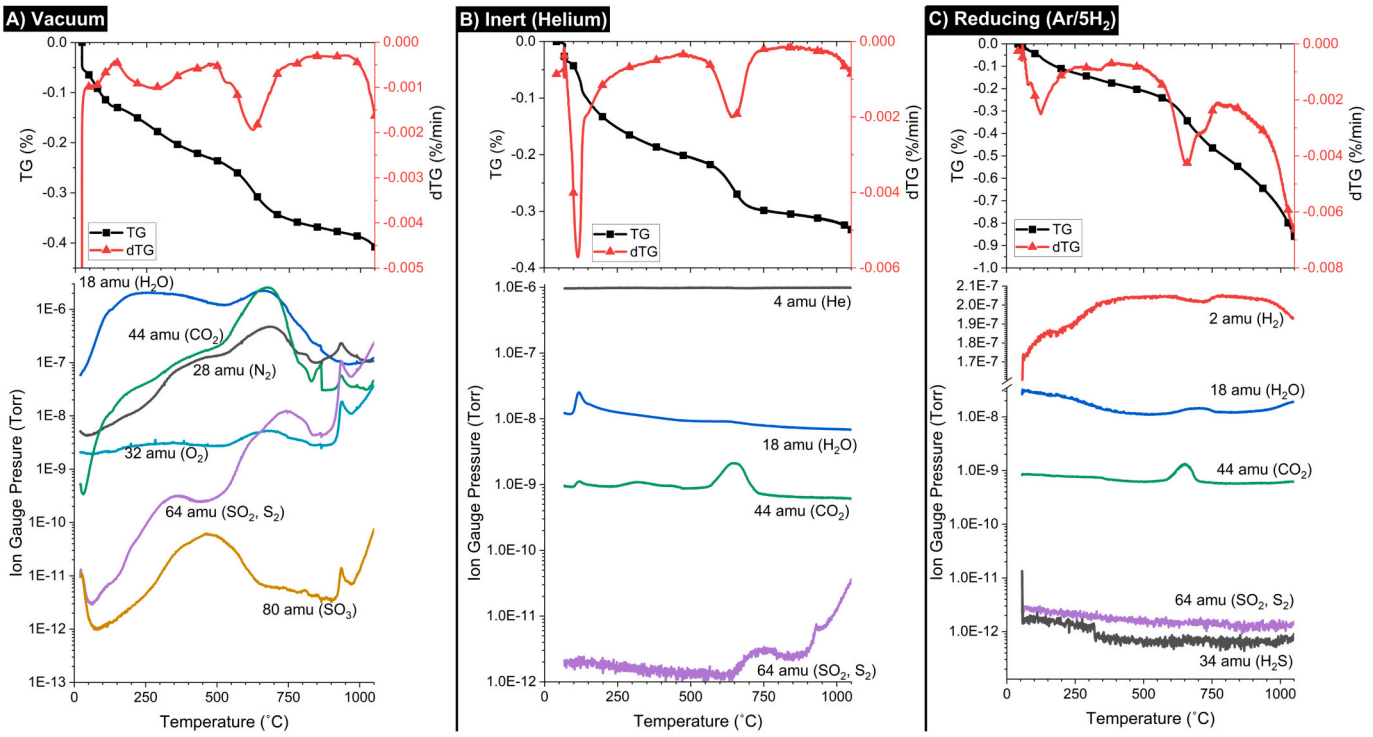


**Fig. 2.** TG-MS curves of JSC-1A heated to 1050°C to avoid vitrification in A) vacuum, B) inert gas, and C) reducing environment. Vacuum and inert show similar gas evolutions, though with higher fidelity vacuum with comparable mass losses in the TG signal. The presence of $H_2$ during heating dramatically increases the total mass loss, the mass loss profile, as well as the composition of the evolved gases. Using the $H_2$ and $H_2O$ traces in reducing atmosphere, it can be seen that there are additional reactions consuming $H_2$ from the gas stream and producing $H_2O$, indicating some oxygen containing components of the simulant are being reduced in these environmental conditions.

**Table 2**
Carbon and sulfur analysis on untreated JSC-1A as well as the 1050°C tests from Fig. 2 in different atmospheres. Predictably, both C and S contents drop after treatment, associated with the evolution of $CO_x$ and $SO_x$ species from carbonate and sulfate decomposition.

| | Untreated | 1050°C He | 1050°C vacuum | 1050°C Ar/$H_2$ |
|---|---|---|---|---|
| Carbon (wt%) | 0.0253 (22) | 0.0064 (3) | 0.0081 (4) | 0.0069 (19) |
| Sulfur (wt%) | 0.0100 (19) | 0.0046 (25) | 0.0036 (8) | 0.0037 (14) |

little impact from gas environment as well, resulting in a 50% reduction in total sulfur. Residual sulfur within the simulant can be attributed to a few different sources. Specifically, as more stable trace sulfides, dissolved sulfates/sulfides in the glass network, or as gaseous species ($S_2$, $SO_x$) trapped within fluid inclusions. Residual carbon can also be attributed to similar dissolved carbonates in the volcanic glass or as trapped $CO/CO_2$ in fluid inclusions still preserved in the glass and mineral phases.

Mössbauer spectrum analysis of the untreated sample indicated the presence of several different chemical environment and oxidation state of Fe. The fitted spectrum (Fig. 3A, also see Table 1) revealed the presence of spectral components related to olivine, Ca-rich clinopyroxene, iron chromite and $Fe^{3+}$ component (most likely arising out of a glassy component) and a broad sextet (from isolated clusters of $Fe^{3+}$). The isomer shift (IS or δ) and quadrupole splitting (QS or $\Delta E_Q$) values indicate presence of $Fe^{2+}$in the two crystallographically different sites, M1 (δ = 1.14(2) and $\Delta E_Q$ = 3.05(2) mm/s) and M2 (δ = 1.13(2) and $\Delta E_Q$ = 2.83(2) mm/s) of olivine structure type in almost equal percentages. The IS and QS vales of olivine are in agreement with the reported values (Recham et al., 2008; Thierry et al., 1981). Similar to the olivine, there is clear evidence of presence of $Fe^{2+}$-containing clinopyroxene compositionally closer to the diopside end members where $Fe^{2+}$ is present in both M1 (δ = 1.16(2) and $\Delta E_Q$ = 2.29(4) mm/s) and M2 (δ = 1.14(2) and $\Delta E_Q$ = 1.91(2) mm/s) sites with an unequal substitution in ~7:11 ratio (de Grave and Eeckhout, 2003). Though such distribution of $Fe^{2+}$ in the two inequivalent sites solely from Mössbauer data has to be interpreted with a bit of caution as it is well-known that Ca deficiency in the M2 site often leads to anomalously larger relative area for the M2 doublet than that anticipated from the actual stoichiometry (Abdu and Hawthorne, 2013; Williams et al., 1971). The IS and QS values for clinopyroxene agree well with the reported values in the literature (Abdu and Hawthorne, 2013; Maksimova et al., 2020). Besides olivine and pyroxene phases, the fitted Mössbauer spectrum also has a component (δ = 0.89(2) and $\Delta E_Q$ = 1.99(2) mm/s) that can be assigned to the $Fe^{2+}$ site arising from spinel type Fe-chromite (Lenaz et al., 2014; Maksimova et al., 2020) and a broad doublet most likely arising from the amorphous $Fe^{3+}$ bearing compositions. The untreated sample also contains a broad hyperfine sextet with IS value of 0.5(4) mm/s and hyperfine magnetic field ($B_{hf}$) of 427.6 kOe, the origin of which is unknown but there could be presence of magnetic phase of $Fe^{3+}$ or isolated cluster of $Fe^{3+}$ as seen in some silicate glass matrix (Bingham et al., 1999; Kukkadapu et al., 2003).

The spectra of vacuum-heated and heated under He atmosphere at 1050°C samples (Fig. 3B and C and Table 1) show noticeable difference as the emergence of curved baseline due to the broad sextet indicating the presence of larger amount of isolated $Fe^{3+}$ clusters due the crystallization of isolated $Fe^{3+}$ species. Other noticeable difference is the absence of $Fe^{2+}$ in a typical chromite phase. We also note that the linewidth of the pyroxene has substantially increased which is due to rearrangement of the next nearest neighbor (NNN) configuration around the M1 site due to different disordering of $Fe^{2+}$ and $Ca^{2+}$ at the neighboring M2 sites as a result of heating at high temperature (Abdu and Hawthorne, 2013). The most significant change in the Mössbauer spectrum, however, is observed for sample heated under reducing condition at 1050°C in 5%$H_2$/Ar (Fig. 3D and Table 1). The spectrum of

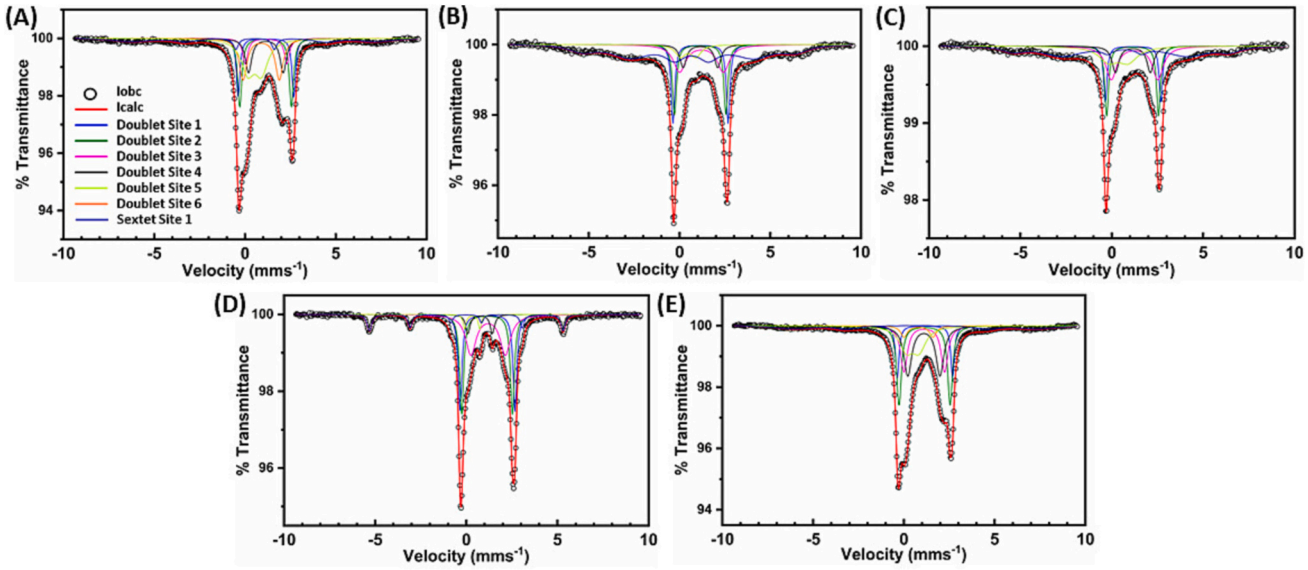


**Fig. 3.** Mössbauer spectra for (A) untreated sample, (B) heated at 1050°C under vacuum, (C) heated at 1050°C under He flow, (D) heated at 1050°C under $Ar/H_2$ and (E) heat treated (heated to 750°C in He and then held for 2 h at 750°C in $Ar/5H_2$) with curve fitting and peak deconvolution. Note the enhancement of doublet site 1 for second and third treatments which indicate an enhancement of the olivine M1 site occupancy by $Fe^{2+}$. Also immediately apparent is the appearance of a sextet peak set in (D) indicative of metallic Fe within the simulant.

reduced sample has a flat baseline with a sextet which can be clearly assigned to metallic Fe phase ($\delta = -0.003(5)$ mm/s and $B_{hf} = 329.41$ kOe). Olivine remained same with almost equal amount of M1 and M2 site population by $Fe^{2+}$, on the other hand diopside can be modelled with one broad doublet ($\delta = 1.20(2)$ and $\Delta E_Q = 1.89(2)$ mm/s). Besides these, there are signature small amount of $Fe^{+3}$ and a $Fe^{2+}$ in the reduced sample probably coming from a spinel type phase(s). It is important to see that the signature of isolated $Fe^{3+}$ cluster is completely absent in the reduced sample presumably transformed in pure iron (alpha-Fe).

### 3.3. Heat treatment design

Using lessons learned from the chemical analysis of the near-vitrification TGA-MS experiments, a lower temperature heat treatment schedule was devised to maximize the amount of non-lunar minerals that are removed while also attempting to preserve the underlying minerology and morphology. Given that $Ar/5H_2$ reducing gas had been

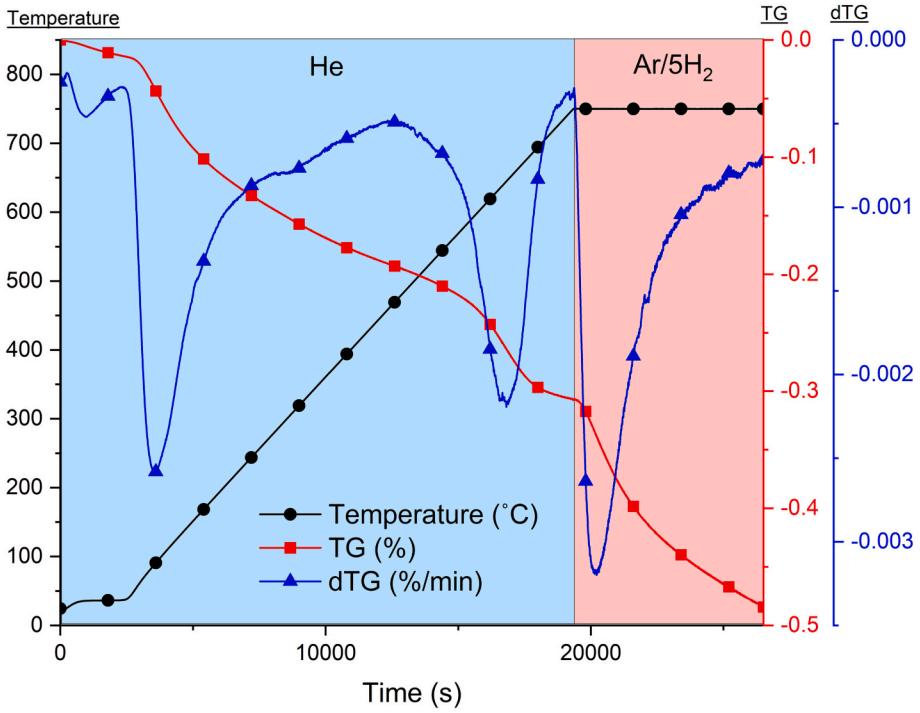


**Fig. 4.** TG of idealized heat treatment schedule of JSC-1A. The evolution of physisorbed and chemisorbed $H_2O$ as well as the evolution of $CO_2$ are done under inert atmosphere, while minor sulfate and oxide reductions occur under reducing conditions at the hold temperature of 750°C. A total mass loss target of 0.50 wt% was achieved by the end of the isothermal section.

shown to reduce the amount of $SO_x$ species evolving at temperatures >800°C, and to potentially form metallic iron in-situ, some or all of the thermal profile would likely including reducing gas. However, the $CO_2$ that outgasses during the carbonate decomposition can react with $H_2$ to form CO or free C. The former of which presents a hazard for upscaling this process, the latter of which is undesirable to have remain in the simulant post-heat treatment. Fig. 4 presents a more idealized final heat treatment for these constraints. Initial heating rate was 2.5°C/min to 750°C in 20 ml/min of flowing He, though Ar would also be an acceptable replacement. $Ar/5H_2$ was then introduced at 750°C and allowed to hold at temperature for two hours. Conceptionally this allows the heat treatment to capture the suspected sulfide/sulfate reduction as well as some amount of iron mineral reduction during the isothermal hold. A two hour hold time was selected to allow reduction to slow to <0.001 wt%/min of mass loss, aiming for a target of 0.5 wt% total mass loss on the TG signal. Ideally this will capture most, if not all, of the nonlunar contaminants as well as enhance iron content to a small degree in the simulant.

### 3.4. X-ray diffraction and phase analysis

After the heat treatment in Fig. 4 was finalized, it was important to determine the unintended consequences of the treatment. One of the primary concerns was the preservation of the igneous mineralogy of the JSC-1A that acts as a simulant for lunar mineralogy. Powder x-ray diffraction was performed between as-received JSC-1A and heat treated JSC-1A according to the new idealized treatment. Fig. 5 shows both diffraction spectra with major and minor peaks indexed. Both spectra were indexed to the same primary mineral phases in the ICDD PDF 4+ database (Gates-Rector and Blanton, 2019). The primary phase found was a plagioclase (PDF 01-073-6461) in the labradorite-bytownite family (66% anorthite, 34% albite). The next most prevalent phase was a high magnesium olivine (PDF 04-011-6662) with a composition of 82% forsterite and 18% fayalite. The final identifiable phase via XRD was a Ca rich clinopyroxene (PDF 00-041-1370) in the diopside family. While there are other reported trace phases (Schrader et al., 2008), only the major ones were able to be identified with XRD. Between the untreated and heat treated JSC-1A, there does not seem to be any major changes in phase composition, though there does seem to be some changes in nominal peak intensity. Specifically, the secondary phases of olivine and clinopyroxene have improvements in their peak intensity while there is some reduction in the plagioclase intensity. Given the increase in background level, it is likely that there is a mild increase in glass content at the expense of a small amount of plagioclase due to vitrification. In parallel, the improvement in olivine and clinopyroxene would indicate some amount of crystal growth in these secondary phases. However, these changes seem to be minor, with the three primary phases being preserved.

Additionally, the Mössbauer spectrum of the heat treated sample is qualitatively similar to the untreated sample (Fig. 3E and Table 1) except some subtle changes on the IS and QS values and the changes in the ratio of Fe in M1 and M2 sites of olivine and diopside. Due to the heat treatment, a reduction of glassy phase and the iron chromite phase is also noticed. This is not surprising as both olivine and clinopyroxene phases are known to undergo disordering and cation movements between M1 and M2 sites at high temperatures (Maksimova et al., 2020; Morozov et al., 2006).

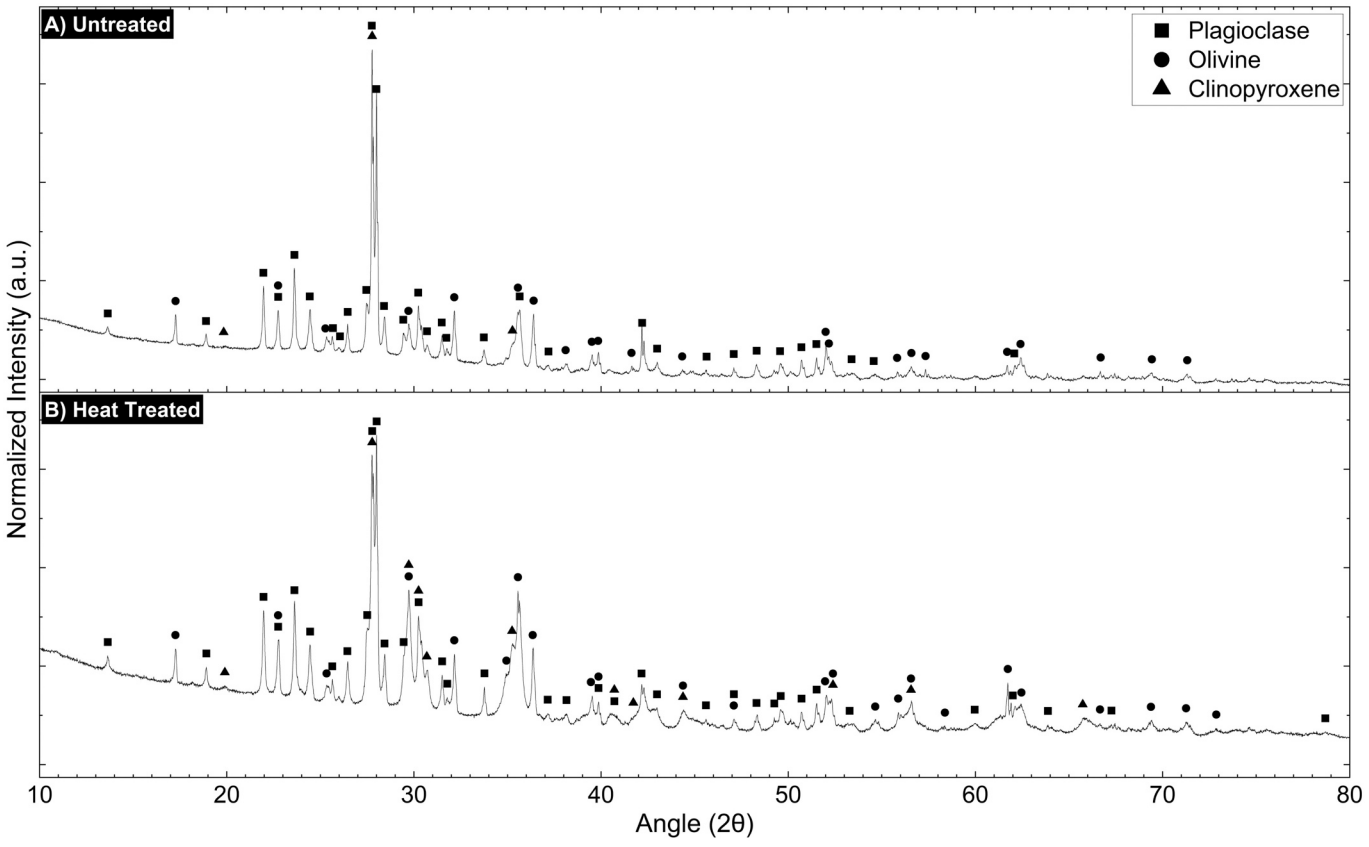


**Fig. 5.** Powder XRD scans of JSC-1A A) untreated and B) after the heat treatment seen in Fig. 4. The same three primary phases were identified as plagioclase, olivine, and clinopyroxene, with trace phases such as titanomagnetite and chromite masked by the major phase peaks. While both untreated and treated JSC-1A indexed to the same phases, after heat treatment has a more significant background, and certain intensities have changed. Notably, the primary phase of plagioclase has some peak reductions while olivine and clinopyroxene have minor enhancements of the major intensities.

### 3.5. Size and morphology analysis

While this heat treatment that has been developed seems to preserve the bulk mineralogy while also removing nonlunar contaminants, changes to the underlying milled powder properties was also important to quantify. The heat treatment at 750°C is above the reported softening point (732°C) (Ray et al., 2010) for JSC-1A derived glass, which means it is absolutely possible for viscous flow of the volcanic glass that comprises ~40 vol% of the total simulant. Fig. 6 are the results of laser diffraction particle size analysis comparing JSC-1A before and after this heat treatment process. Immediately noticeable is that both treated and untreated JSC-1A exhibits a bimodal particle size distribution curve. This matches well with what has been seen in prior research (McKay et al., 1994; Momi et al., 2021) and is likely a result of the milling procedures used to fabricate the simulant. There is only a minor shift in the cumulative PSD curve, indicating that the heat treatment does not dramatically change the particle size distribution. While the volume fraction binning shows that there is a consumption of finer particles from the decrease in the smaller particle size of the bimodal peaks. The heat treated volume fraction binning shows an increase in the particles in the larger particle size of the bimodal peaks, logically showing that fines are being consumed to coarsen the larger particles.

Table 3 provides more quantitative information on these powder characteristics. The D10, D50, and D90 distribution percentiles all see a shift towards larger particle size after heat treatment. Given how wide the distribution for JSC-1A from the single microns all the way to 100 s of microns, a shift of ~20 μm in the D50 is small enough to be acceptable for the needs of this treatment. BET derived powder surface area shows a significant drop before and after heat treatment, reducing surface area by 74%. This can be attributed to two sources. First and foremost, the consumption of fines as seen in the PSD, which account for the highest surface area to volume ratio particles, so even the small total volume they comprise has a significant impact on total surface area. Additionally, particle morphology is expected to change to a degree, with sharp angular features of as-milled JSC-1A getting partially smoothed as the glassy component of the simulant attempting to form more energetically favorable shapes, ideally spheres but more realistically simply "less angular" iterations of the existing particles. The final thing to note is the slight increase in apparent density after heat treatment. Apparent density includes any entrapped porosity as vesicles from the original volcanic rock, so any fining of these out of the glass during heat treatment would enhance apparent density. Given that the treatment is only ~20°C above softening point, glass viscosity is still very high, and glass bubbles that would remain in these powders would be smaller than the particles they are included in, meaning mobility would be even further reduced by the small size. The more likely explanation for the increase in density would be supported by the XRD data: that there is some reduction in plagioclase content and an increase in amount of olivine and clinopyroxene. The plagioclase of the Ca:Na ratio matched in the XRD would be near 2.71 g/cm$^3$, while olivine and the clinopyroxene would be 3.25 g/cm$^3$ and 3.30 g/cm$^3$ respectively. The total composite apparent density would therefore increase with the consumption of the less dense plagioclase and crystallization/growth of the denser olivine and clinopyroxene.

**Table 3**
Cumulative distribution bins from particle size analysis as well as surface area from BET for untreated and heat treated JSC-1A.

| | Untreated | Heat treated |
|---|---|---|
| D10 (μm) | 21.72 | 22.68 |
| D50 (μm) | 108.6 | 129.8 |
| D90 (μm) | 351.2 | 336.8 |
| Surface area (m$^2$/g) | 1.007 (7) | 0.262 (12) |
| Apparent density (g/cm$^3$) | 2.91 | 2.97 |

Fig. 7A and B show the KDE contours in this *AR* vs *FF* space for the respective untreated and heat treated JSC-1A. Contour space for both are bounded by the idealized elliptical particle, as expected. Both contour sets look similar, which is a good initial verification that there are not drastic changes in morphology. The median values do see minor enhancements towards improved aspect ratio as well as improved form factor. This indicates there is some degree of rounding of particles during the heat treatment.

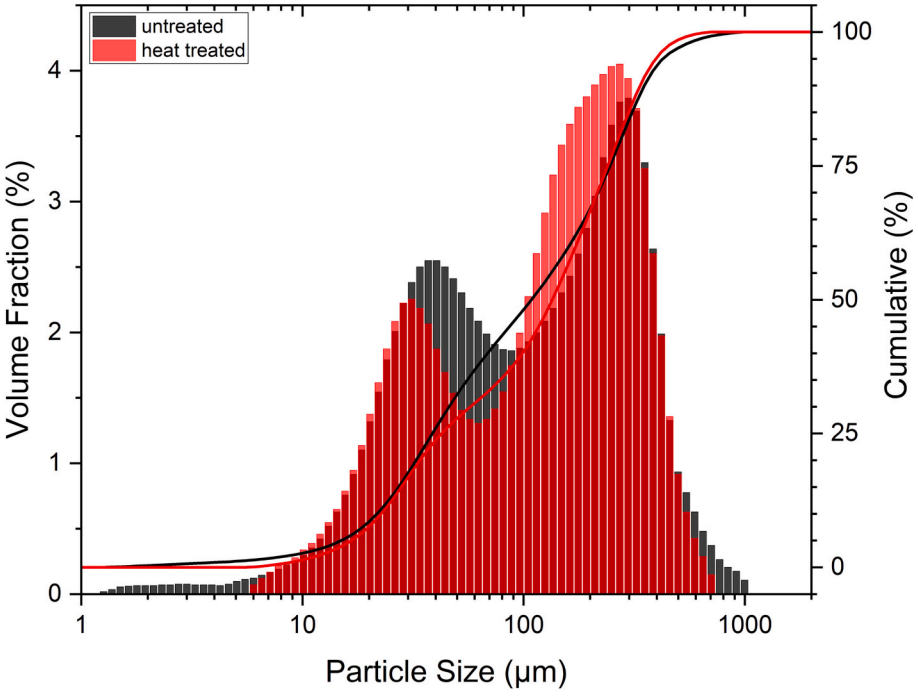


**Fig. 6.** Particle size distribution curves as fractional and cumulative for both untreated and heat treated JSC-1A. Notably the cumulative curve for heat treated JSC-1A has shifted towards coarser particles, and comparing the fractional bar chart shows that this is likely due to the loss of fines (< 5 μm) being consumed into larger particles.

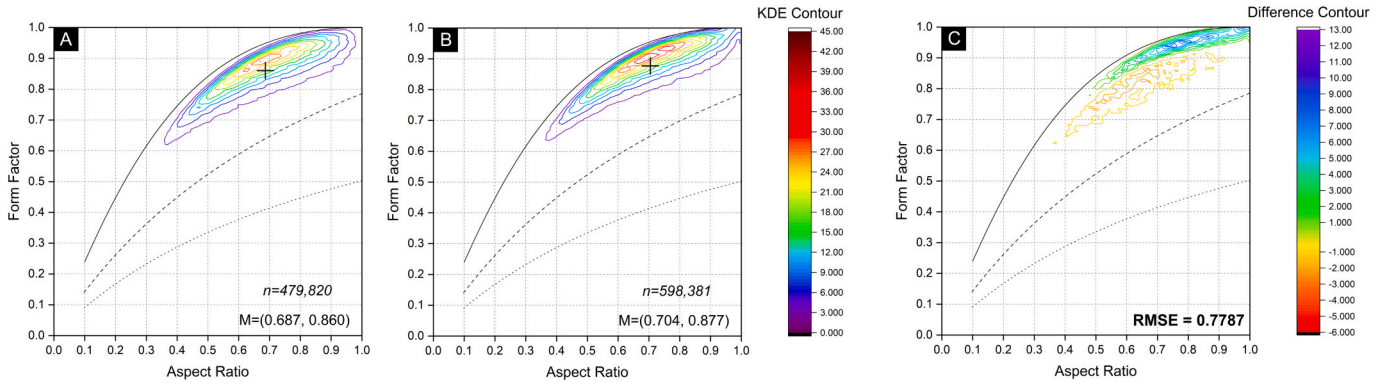


**Fig. 7.** Contour plots of the bivariant kernel density estimates of particle form factor vs. aspect ratio for A) untreated JSC-1A, B) heat treated JSC-1A, and C) the difference (B-A) between the two contours. The median values are marked on the figures with a +, the curves represent form factor and aspect ratio for elliptical particles (solid), rectangular particles (dashed), and rectangular particles with 25% enhanced perimeter (dotted). The median values show an improvement to both form factor and aspect ratio from untreated to treated, while the difference contours show the particles on average are moving towards elliptical nature after heat treatment given the positive contouring near the elliptical line and negative contouring in the space region below.

The RMSE computed to 0.7787, which more distinctly quantifies that there are differences between the untreated and heat-treated powders, however this is low for an RMSE, which gives a degree of confidence that total changes are not major. These differences can be more easily visualized from the difference contour produced by Eq. 4, seen as Fig. 7C which shows distinctly where these changes are occurring. Positive contour intervals can be seen closer to the elliptical bounding line, while negative contours sit at lower form factor and aspect ratio areas, indicating particle rounding and clustering, likely due to the onset of softening (Ray et al., 2010) in the glass component. This is further confirmation that particles are rounding during this heat treatment process, consuming the more highly angular grains.

Finally, SEM images were collected on epoxy mounted powder specimens on untreated and heat-treated JSC-1A, shown in Fig. 8. Backscatter imaging provided optimal phase contrast between the different mineral phases, with the specific phases being identified via EDS. Plagioclase, olivine, and the volcanic glass phases are readily identifiable with only a few trace phases like titanomagnetite being found. Very little in major differences can be ascertained between the untreated and heat-treated JSC-1A mineralogically. A qualitative analysis would show less fines and more particle rounding in the heat-treated powders. However, this could easily be a resulting of mounting and sampling variability and accentuates the importance of more statistically relevant analyses like laser diffraction particle size analysis and dynamic image analysis for particle size and morphology.

## 4. Discussion

Attempting to make lunar simulant more lunar-like in behavior and composition is obviously not always straightforward and is a multifaceted problem. A heat treatment like the one described in this body of work does an excellent job of removing non-lunar contaminants in the form of weathering species from the original Merriam Crater feedstock. However, there are noticeable changes in the underlying mineralogy, particle size distribution, and particle morphology that need to be considered. Fortunately, minimal changes in mineralogical phase compositions are tolerable, as not only does the source material vary in composition, but lunar regolith is not a homogenous composition either. Variability from the norm is expected, so small changes in phase composition still maintain the simulant within specification. PSD and morphology are a more difficult issue to resolve. When considered from just a PSD perspective, it could be argued that the treatment actually

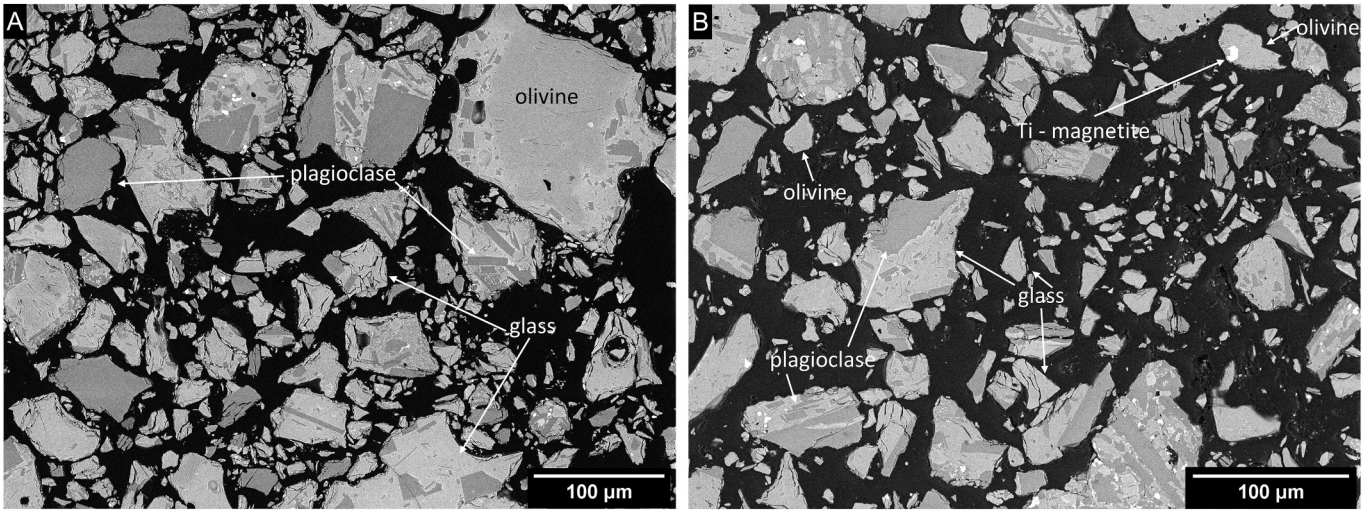


**Fig. 8.** SEM backscatter images of JSC-1A A) untreated and B) heat treated. In both images representative phases were identified with EDS and labeled. Notably clinopyroxenes are known to be present from XRD but phase contrast is identical to the underlying glass and can only be identified by elevated Mg and Ca signals. The images do not show immediately noticeable changes to minerology, and morphological changes can only be identified via large statistical individual particle analysis. However, an cursory look at the particles does seem to indicate that there are less fines, which would agree with the previous particle size and BET data.

drives the simulant closer to lunar PSD, as the bulk of true lunar regolith is a bit larger (Carrier, 2003; Carrier et al., 1973; McKay and Blacic, 1991). Though, both PSD and density are still within the reported lunar norms, and it is also worth noting that much of the referenced PSD for lunar materials was collected via sieve analysis, which tends to skew the results lower due to sieve analysis intrinsically being a measure of the two short axes of particles. However, lunar dust consists of much smaller fines than the bulk of lunar material, and if this treatment is potentially causing local agglomeration by softening and binding the glassy constituents as well as consuming fines then it would suggest the treatment could make JSC-1A potentially less lunar-like, though it should be noted that lunar regolith PSD and composition are not ubiquitous across the lunar surface.

Morphology is another consideration, and unfortunately there are no direct comparisons that can be used at this time. Agglutinates that are unique to lunar soil are difficult to replicate but are known to be highly irregular and tortuous in their morphology. Until such time that large, statistically relevant datasets of the morphology of lunar regolith are produced, the best that can be done is speculate on other known aspects of the morphology. It is well reported that the interior of lunar regolith grains can have tortuous, vesicular structures (Heiken, 1975; Liu and Taylor, 2011). However, the presence of volcanic glass and impact glass has been shown to produce highly rounded grains or smoothed to a certain extent by the melt glass (Heiken, 1975; Yan et al., 2022). While it might be impossible to perfectly replicate the complex vesicular structure that exists in regolith, especially with Fig. 8 confirming that JSC-1A has no internal porous structure, geotechnical properties such as angle of repost, flowability, and rheology (Schrader, 2009) will be more dependent on external morphological features of the grains. As such, the morphological changes from this treatment are believed to make the simulant more lunar like in behavior until such a time that a similar analysis on Apollo or other lunar samples can verify or deny it.

Unfortunately, outside of the Figure of Merit (Schrader et al., 2010), there is no way to quantitatively evaluate the fidelity of regolith simulants. The data at this point does not exist to make a detailed analysis necessary to get an FoM value. To a large degree this is subjective based off the combined experience and knowledge of the authors. Notably though with the FoM technical report, the major factors they considered for simulant fidelity were composition, morphology, density, and PSD. Given that the process clearly subdues non-lunar mineralogy to the extent various phases are removed and minerals changed, the morphology is likely driven towards lunar-like, and that density and PSD are still within reported ranges, there is persuasive evidence that the overall change to increase fidelity for at least some applications. However, the converse maybe true for others and their own applications. As always, it needs to be recognized that the end use of the simulant will really drive if it is appropriate for use and if a heat treatment like what is described here is appropriate.

Scalability and availability of facilities to perform this heat treatment process for researchers is also something to be considered. The use of helium as an inert carrier gas is expensive and arguably unnecessary for a process like this and argon is an appropriate, more readily accessible substitute. Helium was used in the TGA experiments primarily due to reducing buoyant drift of the microbalance as well as the ease of discrimination within the mass spectrometer signals. This process with argon as an inert carrier is easier to facilitate the introduction of pre-blended forming gas or by feeding hydrogen into the argon gas stream which will hopefully make it more accessible to laboratory researchers using a benchtop equipment such as a tube furnace. The NASA Moon-to-Mars Planetary Autonomous Construction Technology (MMPACT) project has also demonstrated larger scalability of this heat treatment with commercial partners using kilns. They have heat treated hundreds of kilograms of JSC-1A with reproducibility to what has been shown within this study.

There is also the original concern of melt bubbling in high temperature vacuum conditions that encouraged this body of work. The original hypothesis of this testing was that the non-lunar contaminants from terrestrial sourced simulant feedstock was the culprit for melt bubbling. However, through further review it is believed to be a more complex nature than expected. Basaltic rock, like those that make up the lunar regolith and the Merriam Crater from which JSC-1A is sourced, are prone to fluid inclusions from natural gasses dissolved in original magma (Heide, 1991; Heide and Schmidt, 2003). These could very well remain in the milled feedstock that ultimately became JSC-1A. This is therefore lunar-like behavior, as even Apollo specimens exhibited similar melt outgassing attributed to the “rupturing of vesicles and gas-rich inclusions” (Gibson, 1973). The other suspected source of melt bubbling is the dissolution of dissolved sulfates in the glass network. It has been noted (Shelby, 2007) that sulfate solubility decreases with increasing temperature, but also overall sulfur solubility decreases with reduced oxygen partial pressure. Both conditions are being met for reduced solubility, vacuum pressure will enhance bubble size and mobility, and MS $SO_x$ signals during and before bubbling like seen in Fig. 1 all support this conclusion. This combination of reduced gas solubility and enhancement of vacuum pressure of bubble growth has recently been noted as a likely candidate for these bubbling phenomena in JSC-1A (Lim et al., 2023), and likely holds true for most lunar regolith simulants. Hence, while the heat treatment is effective at removal of non-lunar species, it does not completely solve the problem of bubble formation once vitrification of mineral species accelerates.

## 5. Conclusions

It has been shown that a simple heat treatment schedule can be used to remove nonlunar weathering species from JSC-1A. While this heat treatment does have some deleterious effects on the lunar simulant, these impacts are considered minimal and overall, the simulant is more lunar-like than in the as-received state. JSC-1A as well as other lunar simulants are expected to still outgas and bubble in high temperature vacuum conditions near and above the vitrification point of the mineral constituents. This indicates that ISRU processes on the moon will need to maintain tight process control if operating in the hard vacuum at the lunar surface as this behavior is expected to also be paralleled by lunar regolith. This could negatively impact consolidation methods that rely on glassification of lunar regolith, and indicates that less mature regolith will likely be more prone to these issues than more mature regolith as they have undergone less micrometeroid weathering and agglutination. It is very likely that construction or consolidation methods will have a higher degree of success if they take advantage of lunar sites that have more mature regolith, less glass, and have accurate temperature and other process feedback streams to avoid overheat events.

## Declaration of Competing Interest

The authors declare that they have no known competing financial interests or personal relationships that could have appeared to influence the work reported in this paper.

## Data availability

Data is available on request from the corresponding author.

## Acknowledgements

The authors would like to thank Gabriel Demeneghi of NASA Marshall Space Flight Center for his microscopy work as well as Richard Boothe of NASA Marshall Space Flight Center for the morphological data acquisition and James Morgan for the carbon/sulfur analysis. This work was funded by the Moon-to-Mars Planetary Autonomous Construction Technology (MMPACT) project within the Microwave Structure Construction Capability element through the Space Technology Mission Directorate (STMD). Part of this work was performed by the Jet

Propulsion Laboratory, California Institute of Technology, under contract with the National Aeronautics and Space Administration.

## References


Abdu, Y.A., Hawthorne, F.C., 2013. Local structure in C2/c clinopyroxenes on the hedenbergite (CaFeSi2O6)-ferrosilite (Fe2Si2O6) join: a new interpretation for the Mossbauer spectra of Ca-rich C2/c clinopyroxenes and implications for pyroxene exsolution. Am. Mineral. 98, 1227–1234. https://doi.org/10.2138/am.2013.4328.

Allen, C., 1993. New lunar simulant available. Space Resour. News 2, 1–2.

Allen, C.C., Morris, R.V., McKay, D.S., 1996. Oxygen extraction from lunar soils and pyroclastic glass. J. Geophys. Res. E Planets 101, 26085–26095. https://doi.org/10.1029/96JE02726.

Bingham, P.A., Parker, J.M., Searle, T., Williams, J.M., Fyles, K., 1999. Redox and clustering of iron in silicate glasses. J. Non-Cryst. Solids 253, 203–209. https://doi.org/10.1016/S0022-3093(99)00361-0.

Bland, W., Rolls, D., 1998. Weathering: An Introduction to the Scientific Principles. Routledge & CRC Press.

Botev, Z.I., Grotowski, J.F., Kroese, D.P., 2010. Kernel density estimation via diffusion. Ann. Stat. 38, 2916–2957. https://doi.org/10.1214/10-AOS799.

Carrier, W.D., 2003. Particle size distribution of lunar soil. J. Geotech. Geoenviron. 129, 956–959. https://doi.org/10.1061/(asce)1090-0241(2003)129:10(956).

Carrier, W.D., Mitchell, J.K., Mahmood, A., 1973. The nature of lunar soil. J. Soil Mech. Found. Div. 99, 813–832.

de Grave, E., Eeckhout, S.G., 2003. 57 Fe Mössbauer-effect studies of Ca-rich, Fe-bearing clinopyroxenes: part III. Diopside. Am. Mineral. 88, 1145–1152. https://doi.org/10.2138/am-2003-0723.

Duffield, W., Riggs, N., Kaufman, D., Champion, D., Fenton, C., Forman, S., McIntosh, W., Hereford, R., Plescia, J., Ort, M., 2006. Multiple constraints on the age of a Pleistocene lava dam across the little Colorado River at Grand Falls, Arizona. Geol. Soc. Am. Bull. 118, 421–429. https://doi.org/10.1130/B25814.1.

Fateri, M., Meurisse, A., Sperl, M., Urbina, D., Madakashira, H.K., Govindaraj, S., Gancet, J., Imhof, B., Hoheneder, W., Waclavicek, R., Preisinger, C., Podreka, E., Mohamed, M.P., Weiss, P., 2019. Solar sintering for lunar additive manufacturing. J. Aerosp. Eng. 32 https://doi.org/10.1061/(asce)as.1943-5525.0001093, 04019101.

Gates-Rector, S., Blanton, T., 2019. The powder diffraction file: a quality materials characterization database. Powder Diffract. 34, 352–360. https://doi.org/10.1017/S0885715619000812.

Gibson, E.K., 1973. Thermal analysis-mass spectrometer computer system and its application to the evolved gas analysis of Green River shale and lunar soil samples. Thermochim. Acta 5, 243–255.

Goulas, A., Friel, R.J., 2016. 3D printing with moondust. Rapid Prototyp. J. 22, 864–870. https://doi.org/10.1108/RPJ-02-2015-0022.

Gustafson, R.J., 2009. JSC - 1A lunar regolith simulant: availability and characterization. In: Lunar Regolith Simulant Workshop. Huntsville, AL, pp. 1–9.

Heide, K., 1991. The degassing behaviour of natural glasses and implications for their origin. J. Therm. Anal. 37, 1593–1603.

Heide, K., Schmidt, C.M., 2003. Volatiles in vitreous basaltic rims, HSDP 2, big island, Hawaii. J Non Cryst Solids 323, 97–103. https://doi.org/10.1016/S0022-3093(03)00285-0.

Heiken, G., 1975. Petrology of lunar soils. Rev. Geophys. 13, 567–587. https://doi.org/10.1029/RG013i004p00567.

Hill, E., Mellin, M.J., Deane, B., Liu, Y., Taylor, L.A., 2007. Apollo sample 70051 and high- and low-Ti lunar soil simulants MLS-1A and JSC-1A: implications for future lunar exploration. J. Geophys. Res. E Planets 112, 1–11. https://doi.org/10.1029/2006JE002767.

Howe, A.S., Wilcox, B., McQuin, C., Mittman, D., Townsend, J., Polit-Casillas, R., Litwin, T., 2014. Modular additive construction using native materials. In: Earth and Space 2014: Engineering for Extreme Environments - Proceedings of the 14th Biennial International Conference on Engineering, Science, Construction, and Operations in Challenging Environments, pp. 301–312. https://doi.org/10.1061/9780784479179.034.

ISO9276-6, 2008. Representation of Results of Particle Size Analysis - Part 6: Descriptive and Quantitative Representation of Particle Shape and Morphology.

Jolliff, B.L., Wieczorek, M.A., Shearer, C.K., Neal, C.R. (Eds.), 2018. New Views of the Moon. Walter De Gruyter GmbH & Co KG. https://doi.org/10.1515/9781501509537.

Kim, B.S., Sohn, H.Y., 2002. A novel cyclic reaction system involving CaS and CaSO4 for converting sulfur dioxide to elemental sulfur without generating secondary pollutants. 3. Kinetics of the hydrogen reduction of the calcium sulfate powder to calcium sulfide. Ind. Eng. Chem. Res. 41, 3092–3096. https://doi.org/10.1021/ie010995+.

Kukkadapu, R.K., Li, H., Smith, G.L., Crum, J.D., Jeoung, J.-S., Howard Poisl, W., Weinberg, M.C., 2003. Mössbauer and optical spectroscopic study of temperature and redox effects on iron local environments in a Fe-doped (0.5 mol% Fe2O3) 18Na2O–72SiO2 glass. J. Non-Cryst. Solids 317, 301–318. https://doi.org/10.1016/S0022-3093(02)01815-X.

Lagarec, K., Rancourt, D.G., 1997. Extended Voigt-based analytic lineshape method for determining N-dimensional correlated hyperfine parameter distributions in Mössbauer spectroscopy. Nucl Instrum Methods Phys Res B 129, 266–280. https://doi.org/10.1016/S0168-583X(97)00284-X.

Lenaz, D., Andreozzi, G.B., Bidyananda, M., Princivalle, F., 2014. Oxidation degree of chromite from Indian ophiolites: a crystal chemical and 57Fe Mössbauer study. Period. Mineral. 83, 241–255. https://doi.org/10.2451/2014PM0014.

Lim, S., Bowen, J., Degli-Alessandrini, G., Anand, M., Cowley, A., Levin Prabhu, V., 2021. Investigating the microwave heating behaviour of lunar soil simulant JSC-1A at different input powers. Sci. Rep. 11, 1–16. https://doi.org/10.1038/s41598-021-81691-w.

Lim, S., Degli-Alessandrini, G., Bowen, J., Anand, M., Cowley, A., 2023. The microstructure and mechanical properties of microwave-heated lunar simulants at different input powers under vacuum. Sci. Rep. 13, 1804. https://doi.org/10.1038/s41598-023-29030-z.

Liu, Y., Taylor, L.A., 2011. Characterization of lunar dust and a synopsis of available lunar simulants. In: Planetary and Space Science, pp. 1769–1783. https://doi.org/10.1016/j.pss.2010.11.007.

Lowell, S., Shields, J.E., 1991. Powder Surface Area and Porosity. Springer Science & Business Media.

Maksimova, A.A., Petrova, E.V., Chukin, A.V., Oshtrakh, M.I., 2020. Fe2+ partitioning between the M1 and M2 sites in silicate crystals in some stony and stony-iron meteorites studied using X-ray diffraction and Mössbauer spectroscopy. J. Mol. Struct. 1216, 128391. https://doi.org/10.1016/j.molstruc.2020.128391.

Massieon, C.C., Cutler, A.H., Shadmanv, F., 1993. Hydrogen Reduction of Iron-Bearing Silicates, pp. 1239–1244.

McKay, D.S., Blacic, J.D., 1991. Production and Uses of Simulated Lunar Materials. Houston TX.

McKay, D.S., Carter, J.L., Boles, W.W., Allen, C.C., Allton, J.H., 1994. JSC-1: a new lunar soil simulant. In: Galloway, R.G., Lokaj, S. (Eds.), Engineering, Construction, and Operations in Space IV. American Society of Civil Engineers, Albuquerque, NM, pp. 857–866.

Metzger, P.T., Zacny, K., Morrison, P., 2020. Thermal extraction of volatiles from lunar and asteroid regolith in axisymmetric Crank–Nicolson modeling. J. Aerosp. Eng. 33 https://doi.org/10.1061/(asce)as.1943-5525.0001165, 04020075.

Momi, J., Lewis, T., Alberini, F., Meyer, M.E., Alexiadis, A., 2021. Study of the rheology of lunar regolith simulant and water slurries for geopolymer applications on the moon. Adv. Space Res. 68, 4496–4504. https://doi.org/10.1016/j.asr.2021.08.037.

Morozov, M., Brinkmann, C., Grodzicki, M., Lottermoser, W., Tippelt, G., Amthauer, G., Kroll, H., 2006. Octahedral cation partitioning in Mg,Fe2+−olivine. Mössbauer spectroscopic study of synthetic (Mg0.5 Fe2+ 0.5)2SiO4 (Fa50). Hyperfine Interact. 166, 573–578. https://doi.org/10.1007/s10751-006-9347-9.

NASA, 2019. SLS-SPEC-159: Cross-Program Design Specification for Natural Environments. NASA Technical Report Server.

NASA, 2020. Artemis Plan: NASA's Lunar Exploration Program Overview, NASA.

Papike, J., Taylor, L., Simon, S., 1991. Lunar minerals. In: Heiken, G.H., Vaniman, D.T., French, B.M. (Eds.), Lunar Sourcebook: A User's Guide to the Moon. Cambridge University Press, Cambridge, UK, pp. 121–181.

Ray, C.S., Reis, S.T., Sen, S., O'Dell, J.S., 2010. JSC-1A lunar soil simulant: characterization, glass formation, and selected glass properties. J. Non-Cryst. Solids 356, 2369–2374. https://doi.org/10.1016/j.jnoncrysol.2010.04.049.

Recham, N., Casas-Cabanas, M., Cabana, J., Grey, C.P., Jumas, J.-C., Dupont, L., Armand, M., Tarascon, J.-M., 2008. Formation of a complete solid solution between the triphylite and fayalite olivine structures. Chem. Mater. 20, 6798–6809. https://doi.org/10.1021/cm801817n.

Rickman, D.L., Lowers, H.A., 2012. Particle Shape and Composition of NU-LHT-2M. NASA TM.

Rickman, D., Immer, C., Metzger, P., Dixon, E., Pendleton, M., Edmunson, J., 2012. Particle shape in simulants of the lunar regolith. J. Sediment. Res. 82, 823–832. https://doi.org/10.2110/jsr.2012.69.

Rickman, D., Lohn-Wiley, B., Knicely, J., Hannan, B., 2016. Probabilistic solid form determined from 2D shape measurement. Powder Technol. 291, 466–472. https://doi.org/10.1016/j.powtec.2015.10.044.

Schlüter, L., Cowley, A., 2020. Review of techniques for in-situ oxygen extraction on the moon. Planet. Space Sci. 181, 104753. https://doi.org/10.1016/j.pss.2019.104753.

Schrader, C.M., 2009. Overview of figure of merit analyses of simulants and the fit-to-use matrix. In: Regolith Simulant Workshop. Marshall Space Flight Center, Huntsville AL.

Schrader, C.M., Rickman, D.L., Mclemore, C.A., Fikes, J.C., Wilson, S.A., Stoeser, D.B., Butcher, A.R., Botha, P.W.S.K., 2008. Extant and extinct lunar regolith simulants: modal analyses of NU-LHT-1M and -2m, OB-1, JSC-1, JSC-1A and -1AF, FJS-1, and MLS-1. In: Planetary and Terrestrial Mining Sciences Symposium. NORCAT, Toronto, Canada, pp. 7–8.

Schrader, C.M., Rickman, D.L., Mclemore, C.A., Fikes, J.C., 2010. Lunar Regolith Simulant User's Guide.

Shelby, J.E., 2007. Introduction to Glass Science and Technology, 2nd ed. Royal Society of Chemistry, Cambridge. https://doi.org/10.1039/9781847551160.

Siderius, D.W., Shen, V.K., Johnson, R.D., van Zee, R.D., 2013. NIST/ARPA-E Database of Novel and Emerging Adsorbent Materials, NIST Standard Reference Database 205. National Institute of Standards and Technology. https://doi.org/10.18434/T4FW23.

Song, L., Xu, J., Fan, S., Tang, H., Li, X., Liu, J., Duan, X., 2019. Vacuum sintered lunar regolith simulant: pore-forming and thermal conductivity. Ceram. Int. 45, 3627–3633. https://doi.org/10.1016/j.ceramint.2018.11.023.

Song, L., Xu, J., Tang, H., Liu, Jiquan, Liu, Jianzhong, Li, X., Fan, S., 2020. Vacuum sintering behavior and magnetic transformation for high-Ti type basalt simulated lunar regolith. Icarus 347, 113810. https://doi.org/10.1016/j.icarus.2020.113810.

Taylor, L.A., Meek, T.T., 2005. Microwave sintering of lunar soil: properties, theory, and practice. J. Aerosp. Eng. 18, 188–196. https://doi.org/10.1061/(asce)0893-1321(2005)18:3(188).

Taylor, S.L., Jakus, A.E., Koube, K.D., Ibeh, A.J., Geisendorfer, N.R., Shah, R.N., Dunand, D.C., 2018. Sintering of micro-trusses created by extrusion-3D-printing of lunar regolith inks. Acta Astronaut. 143, 1–8. https://doi.org/10.1016/j.actaastro.2017.11.005.

Thierry, P., Chatillon-Colinet, C., Mathieu, J.C., Regnard, J.R., Amossé, J., 1981. Thermodynamic properties of the forsterite-fayalite (Mg2SiO4-Fe2SiO4) solid solution. Determination of heat of formation. Phys. Chem. Miner. 7, 43–46. https://doi.org/10.1007/BF00308200.

Tian, H., Guo, Q., Yue, X., Liu, Y., 2010. Investigation into sulfur release in reductive decomposition of calcium sulfate oxygen carrier by hydrogen and carbon monoxide. Fuel Process. Technol. 91, 1640–1649. https://doi.org/10.1016/j.fuproc.2010.06.013.

Vaniman, D.T., Dietrich, J., Taylor, G.J., Heiken, G.H., 1991. Exploration, samples, and recent concepts of the moon. In: Heiken, G.H., Vaniman, D.T., French, B.M. (Eds.), Lunar Sourcebook: A User's Guide to the Moon. Cambridge University Press, Cambridge, UK, pp. 5–26.

Whittington, A., Parsapoor, A., 2022. Lower cost lunar bricks: energetics of melting and sintering lunar regolith simulants. New Space XX 1–12. https://doi.org/10.1089/space.2021.0055.

Williams, P.G.L., Bancroft, G.M., Bown, M.G., Turnock, A.C., 1971. Anomalous Mössbauer spectra of C2/c clinopyroxenes. Nat. Phys. Sci. 230, 149–151. https://doi.org/10.1038/physci230149a0.

Yan, P., Xiao, Z., Wu, Y., Yang, W., Li, J.H., Gu, L.X., Liao, S., Yin, Z., Wang, H., Tian, H. C., Zhang, C., Wu, S., Ma, H.X., Tang, X., Wu, S.T., Hui, H., Xu, Y., Hsu, W., Li, Q.L., Luo, F., Liu, Y., Li, X.H., 2022. Intricate regolith reworking processes revealed by microstructures on lunar impact glasses. J. Geophys. Res. Planets 127. https://doi.org/10.1029/2022JE007260.

Zocca, A., Fateri, M., Al-Sabbagh, D., Günster, J., 2020. Investigation of the sintering and melting of JSC-2A lunar regolith simulant. Ceram. Int. 46, 14097–14104. https://doi.org/10.1016/j.ceramint.2020.02.212.